Optical pumping of electronic quantum Hall states with vortex light

Deric Session[1,10], Mahmoud Jalali Mehrabad [1,10] ✉, Nikil Paithankar [2,10],
Tobias Grass [3,4], Christian J. Eckhardt [5,6], Bin Cao[1],
Daniel Gustavo Suárez Forero [1], Kevin Li[1], Mohammad S. Alam[1],
Kenji Watanabe [7], Takashi Taniguchi [7], Glenn S. Solomon [8],
Nathan Schine [1], Jay Sau [1,9], Roman Sordan [2] & Mohammad Hafezi [1] ✉

A fundamental requirement for quantum technologies is the ability to coherently control the interaction between electrons and photons. However, in many scenarios involving the interaction between light and matter, the exchange of linear or angular momentum between electrons and photons is not feasible, a condition known as the dipole approximation limit. An example of a case beyond this limit that has remained experimentally elusive is when the interplay between chiral electrons and vortex light is considered, where the orbital angular momentum of light can be transferred to electrons. Here we present a mechanism for such an orbital angular momentum transfer from optical vortex beams to electronic quantum Hall states. Specifically, we identify a robust contribution to the radial photocurrent, in an annular graphene sample within the quantum Hall regime, that depends on the vorticity of light. This phenomenon can be interpreted as an optical pumping scheme, where the angular momentum of photons is transferred to electrons, generating a radial current, and the current direction is determined by the vorticity of the light. Our findings offer fundamental insights into the optical probing and manipulation of quantum coherence, with wide-ranging implications for advancing quantum coherent optoelectronics.

Coherent manipulation of light–matter hybrids plays a crucial role in advancing future quantum technologies and optoelectronics[1,2]. Particularly desirable is the control over the spatial degree of freedom in light–matter interactions. Typically, owing to the presence of disorder or Coulomb binding, electronic wavefunctions are much more spatially confined than the wavelengths of associated optical transitions. Consequently, the light–matter interaction occurs locally, and neither the spatial profile of the optical field nor the spatial extent of the electron wavefunction has a significant influence on these interactions, a regime known as the dipole approximation. In other words, in this regime, only direct optical transitions are accessible, and the transfer of linear and orbital angular momentum (OAM), which enables optical control of the spatial degrees of electrons, is not possible.

To understand this, one can consider a simplified model of a hydrogen-like atom, where the typical Bohr radius (a_B) is much smaller than the corresponding optical transition wavelength (λ). Therefore,

[1]Joint Quantum Institute (JQI), University of Maryland, College Park, MD, USA. [2]L-NESS, Department of Physics, Politecnico di Milano, Como, Italy.
[3]DIPC—Donostia International Physics Center, San Sebastián, Spain. [4]Ikerbasque—Basque Foundation for Science, Bilbao, Spain. [5]Institut für Theorie der Statistischen Physik, RWTH Aachen University and JARA-Fundamentals of Future Information Technology, Aachen, Germany. [6]Max Planck Institute for the Structure and Dynamics of Matter, Center for Free-Electron Laser Science (CFEL), Hamburg, Germany. [7]National Institute for Materials Science, Tsukuba, Japan. [8]Department of Physics and the Institute of Photonics and Advanced Sensing (IPAS), University of Adelaide, Adelaide, South Australia, Australia.
[9]Condensed Matter Theory Center, University of Maryland, College Park, MD, USA. [10]These authors contributed equally: Deric Session, Mahmoud Jalali Mehrabad, Nikil Paithankar. ✉e-mail: mjalalim@umd.edu; hafezi@umd.edu
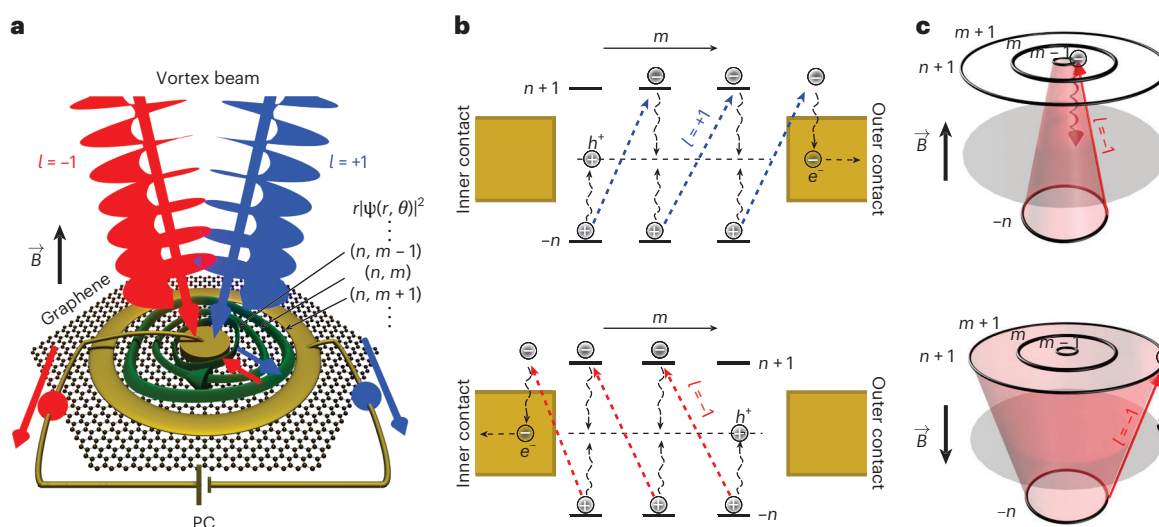
Fig. 1 | Concept of OAM pumping. a, Schematic of LLs in the annular disc geometry subject to the vertically irradiated vortex beam. The green surfaces show representative states within a single LL. The electron distributions in the lowest LLs and directions of the induced radial PC are indicated by arrows. **b**, Optical transitions and PC generation between inner and outer contacts using $\ell = +1$ (blue arrows) and $\ell = -1$ (red arrows) for σ^+ polarized light. For σ^- transitions, see Supplementary Section 7. Light carrying OAM $\ell = +1$ ($\ell = -1$) increases (decreases) m and hence leads to expansion (shrinking) of the spatial

extent of the electronic wavefunction. In this way, the shown scheme realizes an analogue to optical pumping. **c**, Schematic of the photoexcitation transitions between LLs with negative (red arrow) vortex beam in the presence of an upward (top) and downward (bottom) pointing magnetic field. In the top (bottom) panel, the magnetic field is anti-parallel (parallel) to the helicity of light, leading to the shrinking (expansion) of the wavefunction radius. In **c**, only the electron relaxation is considered.

the next-order quadrupole transition is weaker by a factor of $(a_B/\lambda)^2$ than the dipole transition, yet it is still observable in ion trap experiments where ions are excited with OAM beams[3]. In fact, in the dipole approximation regime, most of the imparted angular momentum goes to the centre of mass[4–6] and leads to stirring. Such an effect has been observed both in neutral cold atoms[7] and exciton–polariton systems[8–10].

One approach to go beyond the dipole approximation limit is to shrink the wavelength of the electromagnetic field, which can be achieved by using plasmonic effects[11,12]. Alternatively, if the electronic wavefunction is coherently extended over the associated optical transition wavelength, and electrons are more itinerant than bound, then a gross violation of the dipole approximation is expected. For the case of linear excitation, this can lead to the photon drag effect if the electron–hole binding is weak[13]. The other striking example is the quantum Hall system, where the electrons in two dimensions are subject to a strong out-of-plane magnetic field. Consequently, the kinetic energy is suppressed and electrons exhibit cyclotron motions with chiral characteristics that make it a promising system to investigate the interplay of the chirality of electrons and photons and the transfer of angular momentum in between[14–18].

In particular, there has been a growing interest in investigating chiral and topological effects in photonic systems and also light–matter hybrids[18–21]. Such topological features can be either in the momentum domain and lead to Chern bands, or simply in the spatial degrees of freedom, such as optical vortex beams. Specifically, in addition to spin, in the form of polarization, light can also carry OAM[22,23]. Such an OAM is quantized and given by $\hbar\ell$, where $\hbar$ is the Dirac constant and ℓ is the mode number that determines the phase winding of a vortex beam. The interaction of such vortex beams with materials has led to a plethora of exciting phenomena[24], such as the orbital photogalvanic effect[25]. So far, such studies have not been extended to the quantum Hall regime.

In this work, we experimentally demonstrate the transfer of OAM to electrons in a quantum Hall graphene device with annular geometry using optical vortex beams. In particular, harnessing non-conventional optical selection rules of the Landau levels (LLs) described in Fig. 1c, we show a vorticity-selective light–matter interaction between twisted

light and the electronic wavefunctions manifesting as a radial photocurrent (PC). We show that this radial PC only depends on the vorticity of light as a direct indication of spatially coherent light–matter interaction. We provide further evidence of the robustness of this mechanism by comparison with circularly polarized light. Specifically, we find that the PC contribution from OAM is at least one order of magnitude larger than the contribution of spin angular momentum (polarization), allowing us to confirm the significant role of the beam's spatial topology, and its ability to control the spatial degree of electrons.

To present the motivation and a basic understanding of our experiment, we discuss spatially dependent light–matter interactions that can manipulate the spatial degrees of freedom of electrons within a quantum Hall system. In particular, using an LL picture, we observe how the transfer of OAM from photons to electrons results in a radial current, where the direction of the current is determined by the vorticity of the light. As shown in Fig. 1, we consider optical transitions between two LLs, in the presence of rotational symmetry perpendicular to the plane of the quantum Hall sample. In this scenario, the sample is irradiated by an optical vortex where each photon is carrying an OAM $\hbar\ell$ (refs. 14,16).

During the excitation process, the OAM of $\hbar\ell$ is transferred to electrons[14,16]. As the radius of the electronic wavefunction increases monotonically with angular momentum, this optical transfer of angular momentum causes a radial change in the electronic wavefunction, which is solely determined by the vorticity of the light. The subsequent relaxation process conserves OAM on average and therefore maintains the OAM transfer from the original excitation. This concept is in direct analogy to optical pumping in atomic systems, wherein cyclical pumping among different hyperfine states of bound electrons within an atom transfers them to a specific quantum state[26].

Note that despite the absence of rotational symmetry in the presence of disorder, the optical pumping model continues to hold true[16]. Moreover, the optical pumping picture also provides a simple estimate of the resulting PC: assuming that OAM pumping was the only mechanism of charge transport, the OAM needed to carry one electron through the sample equals the number M of orbitals in an LL, which is given by $M = A/(\pi l_B^2)$, where A is the area of the sample and l_B is the magnetic
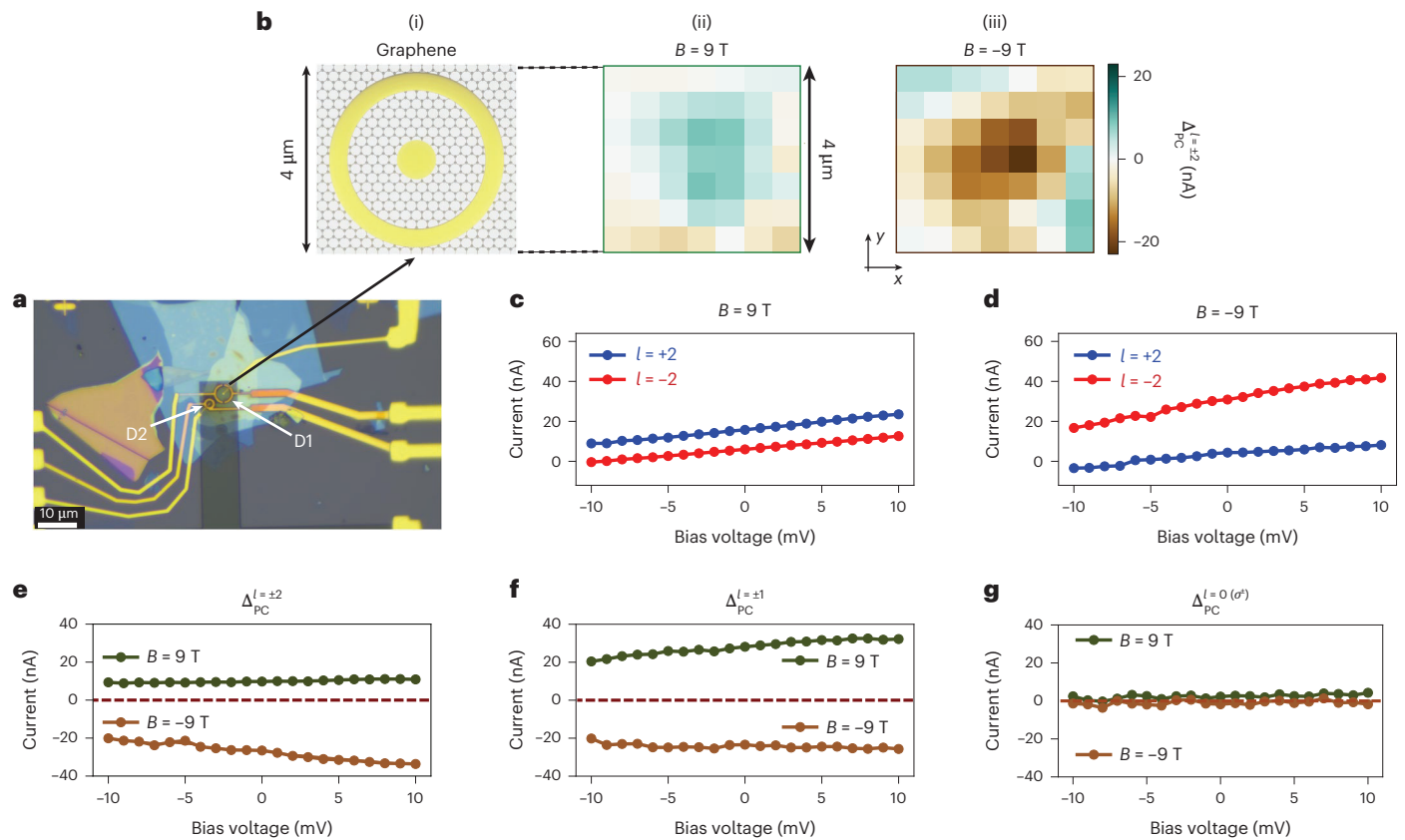
Fig. 2 | OAM-selective PC generation. a, Optical microscope image of the sample, showing two Corbino devices labelled D1 and D2. Corbino D1 has a diameter of ~4 µm and Corbino D2 has a diameter of ~2 µm. D1 is the device used for the data in the main text of this article, for which the inner and outer contacts are marked. The grey rectangle shows the metallic back gate. **b**, (i) Sample schematic and (ii,iii) spatially resolved PC difference Δ_{PC} for $\ell = \pm 2$, at $B = 9$ T and $B = -9$ T, respectively. Bias voltage V_b for both cases was ~4 mV. **c,d**, Measured PC as a function of bias voltage V_b generated using light carrying $\ell = +2$ (blue) and $\ell = -2$ (red) at $B = 9$ T (**c**) and $B = -9$ T (**d**). **e–g**, The Δ_{PC} for $B = 9$ T (green) and $B = -9$ T (brown) for $\ell = \pm 2$ (**e**), $\ell = \pm 1$ (**f**) and $\ell = 0$ (**g**), respectively. In **g**, at each magnetic field, the Δ_{PC} is calculated by subtracting the PC generated using two Gaussian beams with opposite circular polarization ($\sigma^{\pm}$). In all panels, the gate voltage V_g and the average pump power were 1.78 V and 10 µW, respectively. Relative differences of curves within and between **e** and **f** depend on system parameters, which are described in Supplementary Section 4a.

length. The estimated transported charge, δQ, during the time interval δt by N_{ph} photons, is $\delta Q = eN_{ph}\ell/M$. Therefore, for photons with energy $\hbar\omega$, the PC obtained from the laser power $P = \hbar\omega \times N_{ph}/\delta t$ is $I = \delta Q/\delta t = eP\ell/(\hbar\omega M)$. This picture also implies that, upon inverting the direction of the magnetic field, the PC changes direction, as illustrated in Fig. 1c.

Results

Bias voltage dependence of PC

To experimentally demonstrate this mechanism, we use a device consisting of a hexagonal boron nitride (hBN) encapsulated monolayer graphene in an annular (Corbino) geometry as shown in Fig. 2a. The choice of the Corbino geometry allows us to exclusively probe the transport of bulk states. Moreover, the circularly symmetric shape of the Laguerre–Gauss mode profiles optically matches the shape of the sample. The inner and outer contacts are used to apply an in-plane electric field and also measure the generated PC, while the back-gate voltage V_g controls the Fermi level. We apply an out-of-plane external magnetic field up to 9 T at 4.2 K to be in the quantum Hall regime. The optical vortex beams of different vortices ℓ are generated by a spatial light modulator (SLM) and are concentrically focused on the Corbino device (for the sample and optical set-up, see Supplementary Sections 1 and 3). This enables us to excite the carriers in our device, which undergo vorticity-selective optical transitions, shown in Fig. 1c. For all the measurements, we choose $V_g = 1.78$ V, which sets the Fermi energy near filling factor $\nu = 6$.

The generated PC for various optical vortices $\pm\ell$ are independently measured, while the beam is spatially scanned over the sample. Figure 2b shows PC difference (subtracted), Δ_{PC}, where the vortex beam $\ell = \pm 2$ is spatially scanned over the sample (shown schematically in (i)), at (ii) $B = 9$ T and (iii) $B = -9$ T. It can be clearly observed that the Δ_{PC} flips sign when the magnetic field direction is reversed. This remarkable observation corroborates with the earlier optical pumping picture of Fig. 1a, where depending on the vortices of the optical beam the radial extent of the electrons either shrink or expand during the optical excitation. Note that the sign of the observed PC difference depends solely on the phase winding of the optical vortex beam, and not the intensity; therefore, one cannot associate this (beyond the dipole approximation) process with heating.

It is unlikely that any sample has pristine electrical conditions and it may harbour residual or intrinsic in-plane potential. Such inherent potential could potentially explain the presence of a radial PC in the Corbino sample. To rule out the origin of our observed effect to such an in-plane electric field, we apply a bias voltage V_b between the inner and outer contacts to create a controllable potential gradient in the radial direction. Figure 2c,d shows the measured PC as a function of V_b for $B = 9$ T and $B = -9$ T, respectively. Remarkably, we observe multiple unambiguous signatures of the vorticity-selective light–matter interaction. First, as shown in Fig. 2c,d, for $\ell = +2$ (blue) and $\ell = -2$ (red) at each magnetic field, we observe a consistent and significant difference in the generated PC for a wide range of V_b ($-10 \leq V_b \leq 10$ mV). In other
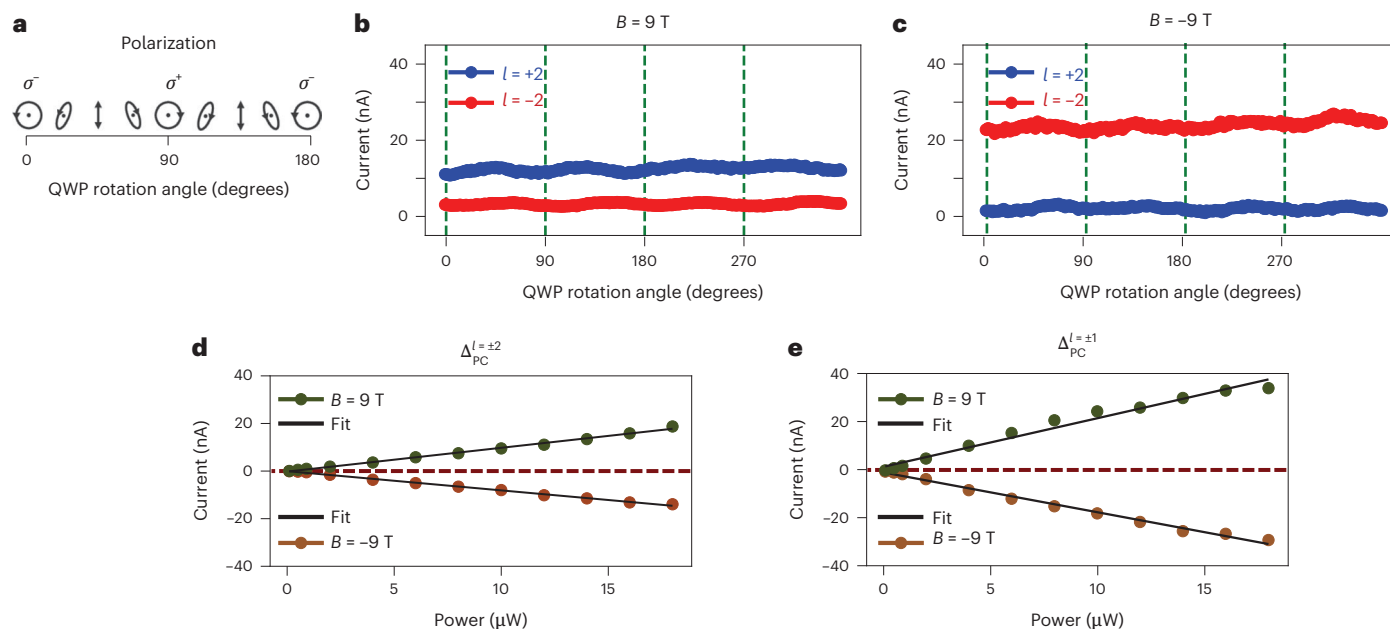
Fig. 3 | Polarization-resolved and power-dependent PC measurements.
a, Polarization of the pump beam as a function of the QWP rotation, shown schematically at the top. σ^+ and σ^- denote the positive and negative circular polarization. Between each consecutive circular polarization, continuous rotation of the QWP changes the polarization periodically from circular to elliptical, to linear polarization. **b,c**, PC measured as a function of QWP rotation using light carrying $\ell = +2$ (blue) and $\ell = -2$ (red) at $B = 9$ T (**b**) and $B = -9$ T (**c**), respectively. The green vertical dashed lines indicate the consecutive σ^+ and

σ^- polarization. All measurements are done at a fixed $V_g = 1.78$ V, $V_b = -4$ mV and an average pump power of 10 μW. **d,e**, Pump power dependence of PC: PC difference Δ_{PC} measured as a function of average pump power using light carrying $\ell = \pm 2$ (**d**) and $\ell = \pm 1$ (**e**) OAM at $B = 9$ T (green circles) and $B = -9$ T (brown circles), respectively. The black lines show the least-squares linear fit. In all of the data presented in the main text, the average pump power was set to 10 μW, at which a linear behaviour is observed.

words, radially tilting the electric potential can change the total PC; however, the PC difference Δ_{PC} remains relatively constant. Second, for the opposite magnetic field, we observe a clear sign flip for the PC difference (Fig. 2e). Specifically, since the OAM is defined relative to the magnetic field, inverting the latter effectively inverts the OAM and should therefore lead to a sign change of the observed radial PC, which is clearly observed in Fig. 2e. In an ideal case, the amplitude of this flipped current should be the same; however, owing to slightly different spatial alignment for different magnetic fields, the magnitude of the PC is different (Fig. 2b, (ii) and (iii)). Third, to investigate the effect of the degree of vorticity on the generated PC, we illuminate the sample with $\ell = \pm 1$ beams. As shown in Fig. 2, robust PC difference $\Delta_{PC}^{\ell = \pm 1}$ is observed across a wide range voltage bias, and the sign reversal with the magnetic field is present. For a large sample subject to the optical vortex, one expects Δ_{PC} to increase with the vorticity degree ℓ (ref. 16). However, we note that our experiment was designed such that the Corbino sample would have an optimal spatial overlap for optical vortex beams with $\ell = \pm 1$. Since the OAM beams with larger vorticity are spatially larger (in free space, the vortex of the OAM beam with $\ell = \pm 2$ is approximately two times larger than that of the beam with $\ell = \pm 1$), the spatial overlap of the sample and optical vortex beam reduces with vorticity. This means that the amount of graphene inside the Corbino that is illuminated decreases with vorticity. This reduction of beam-sample overlap is the main reason why we observe a reduced Δ_{PC} for $\ell = \pm 2$ compared with $\ell = \pm 1$. Moreover, as shown in Fig. 2b, the magnitude of radial PC difference, Δ_{PC}, diminishes as the centre of the beam reaches the outer contact. This indicates that graphene-contact interface effects are not playing a significant role in our observations and the radial PC is dominantly generated from the bulk.

Fourth, to rule out the origin of Δ_{PC} based on circular polarization, the sample is illuminated with $\ell = 0$ beams consisting of two Gaussian beams with opposite circular polarization (σ^+ and σ^-). As shown in Fig. 2g, the PC difference for different circular polarization and $\ell = 0$

is at least an order of magnitude smaller than the non-zero ℓ cases. Therefore, we associate the non-zero radial current with the OAM of light, rather than the spin angular momentum.

Polarization dependence of PC
To further decouple the role of the polarization of the optical field from OAM in our experiments, we perform polarization-resolved PC generation using OAM of light by using a variable quarter-wave plate (QWP) in the excitation path. We rotate the QWP such that the polarization continuously changes from linear to elliptical to circular while measuring the PC (Fig. 3a). The measured PC for $\ell = +2$ (blue) and $\ell = -2$ (red) at $B = 9$ T and $B = -9$ T is shown in Fig. 3b,c.

Here there are three clear observations confirming the robustness of OAM-induced PC generation. First, the OAM-induced PC difference is almost an order of magnitude larger than the amplitude of the current oscillations induced by QWP rotation. Second, the OAM-induced PC difference never changes sign as a function of QWP rotation, further confirming the domination of the observed vorticity-selective PC. Finally, this measurement sheds light on the role of focusing the optical beam on its polarization properties. This is crucial since in our measurements, we focus the beam onto the sample using an aspheric lens with a numerical aperture (NA) of 0.68. This large NA may distort the polarization beyond the paraxial approximation. However, Fig. 3b,c shows that this distortion of polarization is relatively insignificant and it does not affect the validity of our results.

Power dependence of PC
To verify the linear power dependence of the OAM transfer, we also investigate the power dependence of the OAM-induced PC in our measurements as a function of optical pump power by varying the average power of our excitation beam within the range of 0.1–18 μW. Figure 3d,e shows that the generated PC increases linearly with the pump intensity. From the above optical pumping estimate, we have
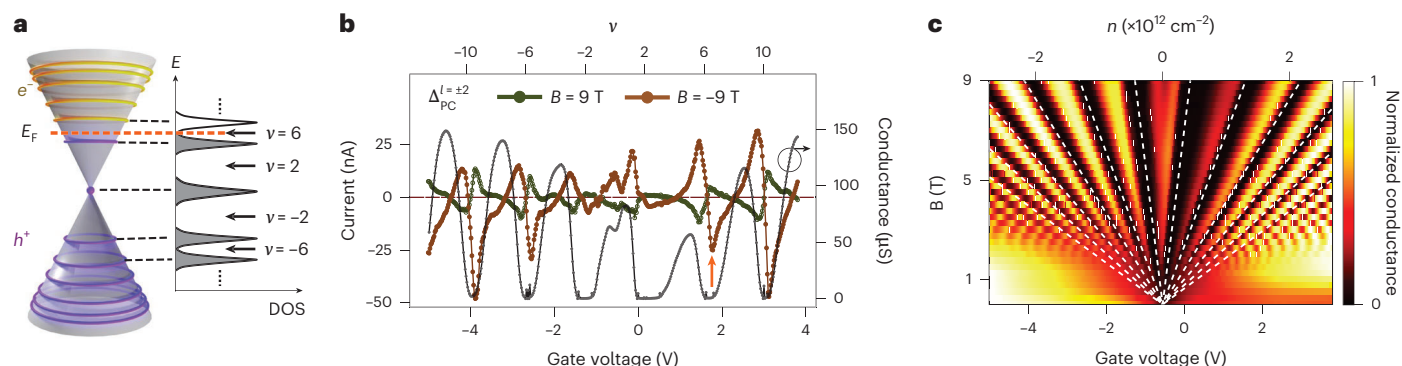
Fig. 4 | Gate voltage dependence of PC. a, Schematic of graphene's band structure near the Dirac point with LLs shown in yellow and purple for the electron and holes, respectively. The inset shows the density of states (DOS) as a function of energy with the Fermi energy. **b**, Measured PC difference as a function of gate voltage using light carrying $\ell = \pm 2$ at $B = 9$ T (green) and $B = -9$ T (brown), respectively. The top x-axis shows the calculated integer filling factors (Supplementary Section 2). The two-terminal longitudinal conductance measured at $B = 9$ T (black circles) is also shown. This measurement was done at

$V_b = -4$ mV and an average pump power of 10 μW. The orange arrow indicates the gate voltage for which all the previous measurements were performed. **c**, Landau fan measured via magneto-transport as a function of the magnetic field, gate voltage (carrier density marked on the top x-axis). The conductance is normalized for each magnetic field value. The white dashed lines denote integer filling factors calculated from the conversion of gate voltage to carrier density (Supplementary Section 2).

$l_B \approx 26$ nm$/\sqrt{B/(1 \text{ tesla})} \approx 9$ nm, and $M = A/(\pi l_B^2) \approx 3 \times 10^4$. The PC is estimated to be $I \approx (0.1 \text{ nA μW}^{-1})P$. Interestingly, the slope of the experimental power dependence (-1 nA μW^{-1}) significantly exceeds this estimate. As we discuss in more detail below, the PC signal also shows a strong gate voltage dependence owing to relaxation effects, and the experimental values are taken at local PC difference maxima, where significant carrier multiplication can be expected[27]. In addition, the donut-shaped intensity profile of the light, not taken into account in the estimate, enhances the current flow into the outer contact. In addition, the OAM-induced PC differences increase linearly with pump power, which indicates that our experiment was performed in the linear regime away from the Pauli blockade in ref. 16.

Gate voltage dependence of PC

Next, we investigate the role of the Fermi energy (E_F) in the generated vorticity-selective PC. By changing the gate voltage V_g, we tune E_F between LLs, that is, we tune the LL filling factor ν. As shown in Fig. 4b, the subtracted PC (for $\ell = \pm 2$) changes sign as a function of V_g, with the direction of PC changing twice between each consecutive conductance peak. In Fig. 4b, green (brown) denotes the subtracted PC at $B = 9$ T ($B = -9$ T), respectively. Such a sign change has also been observed in other quantum Hall graphene systems. This phenomenon has been attributed to a 'bottleneck effect' where the location of E_F with respect to the LLs favours the relaxation of electrons versus holes, and therefore the PC can change sign with V_g (ref. 27). While such an effect was observed in a rectangular geometry to explain the chirality of edge PC, it is likely that the bottleneck effect is also changing the majority carriers in the bulk, and therefore it is relevant to our Corbino geometry. Moreover, a semiclassical scattering analysis (Supplementary Sections 10 and 11) shows that the variation of the longitudinal conductivity near the plateau transition can also contribute to a sign change of the PC.

Discussion

In summary, we demonstrated a mechanism for transferring OAM from photons to electrons. Our OAM optical pumping scheme is analogous to cold-atom and ion optical pumping, and can be used to manipulate itinerant electrons. In addition, our results suggest that the control of spatial degrees of freedom in light–matter interactions can become a new and versatile toolbox in solid-state systems. Generally, our OAM-selective optical pumping picture assumes non-interacting electrons and can be extended to other platforms in which the Coulomb

binding energy is weak and therefore the excitonic Bohr radius remains larger than the field gradient length scale. This approach heralds a new ability to image the spatial coherence of electrons, a fundamentally new probe of quantum materials, inaccessible through existing measurements such as multi-port transport and scanning tunnelling microscopy[28]. For example, our work highlights the potential of using structured light as a powerful tool to monitor the spatial coherence of electronic wavefunctions and its modification to quantum Hall plateau transitions as well as thermal effects. One immediate direction is to use THz fields, as opposed to the optical fields used in our case, to excite the two nearest LLs[29]. The advantage of this approach is the absence of cascade relaxation. Also, the influence of gradient fields on the quantum Hall system has been recently observed in the THz domain, suggesting that this platform is a promising candidate[30]. A more ambitious direction involves the strongly interacting limit, where one could exploit the transfer of OAM to probe fractional quantum Hall states and excite and manipulate anyons[31–35].

Moreover, our experiment provides a unique testbed for investigating the interplay between topology and chirality in the interactions between electrons and photons. While our experiment was performed in the low excitation limit, there are several intriguing proposals to use a strong drive field and exploit the spatially coherent light–matter interaction to induce a wider class of topological insulators in electronic systems by using various structured light[23,36–39]. Furthermore, while our graphene system lacks a photoluminescence response, our scheme can be applied to materials where emission from electronic LLs is possible[40], potentially enabling the observation of chiral photon emission. Another promising avenue is the prospect of coherent wavefunction spectroscopy, where interferometric techniques can be integrated into our experimental scheme to measure and modulate the spatial distribution of wavefunction amplitudes and phases[41].

Online content

Any methods, additional references, Nature Portfolio reporting summaries, source data, extended data, supplementary information, acknowledgements, peer review information; details of author contributions and competing interests; and statements of data and code availability are available at https://doi.org/10.1038/s41566-024-01565-1.

References

1. Bloch, J., Cavalleri, A., Galitski, V., Hafezi, M. & Rubio, A. Strongly correlated electron–photon systems. *Nature* **606**, 41–48 (2022).

2. Basov, D., Fogler, M. & García de Abajo, F. Polaritons in van der Waals materials. *Science* **354**, aag1992 (2016).
3. Schmiegelow, C. T. et al. Transfer of optical orbital angular momentum to a bound electron. *Nat. Commun.* **7**, 12998 (2016).
4. Grass, T., Bhattacharya, U., Sell, J. & Hafezi, M. Two-dimensional excitons from twisted light and the fate of the photon's orbital angular momentum. *Phys. Rev. B* **105**, 205202 (2022).
5. Konzelmann, A. M., Krüger, S. O. & Giessen, H. Interaction of orbital angular momentum light with Rydberg excitons: modifying dipole selection rules. *Phys. Rev. B* **100**, 115308 (2019).
6. Quinteiro, G. F. Below-bandgap excitation of bulk semiconductors by twisted light. *Europhys. Lett.* **91**, 27002 (2010).
7. Andersen, M. et al. Quantized rotation of atoms from photons with orbital angular momentum. *Phys. Rev. Lett.* **97**, 170406 (2006).
8. Boulier, T. et al. Injection of orbital angular momentum and storage of quantized vortices in polariton superfluids. *Phys. Rev. Lett.* **116**, 116402 (2016).
9. Dominici, L. et al. Interactions and scattering of quantum vortices in a polariton fluid. *Nat. Commun.* **9**, 1467 (2018).
10. Kwon, M.-S. et al. Direct transfer of light's orbital angular momentum onto a nonresonantly excited polariton superfluid. *Phys. Rev. Lett.* **122**, 045302 (2019).
11. Andersen, M. L., Stobbe, S., Sørensen, A. S. & Lodahl, P. Strongly modified plasmon–matter interaction with mesoscopic quantum emitters. *Nat. Phys.* **7**, 215–218 (2011).
12. Rivera, N., Kaminer, I., Zhen, B., Joannopoulos, J. D. & Soljačić, M. Shrinking light to allow forbidden transitions on the atomic scale. *Science* **353**, 263–269 (2016).
13. Wieck, A., Sigg, H. & Ploog, K. Observation of resonant photon drag in a two-dimensional electron gas. *Phys. Rev. Lett.* **64**, 463 (1990).
14. Gullans, M. J., Taylor, J. M., Imamoğlu, A., Ghaemi, P. & Hafezi, M. High-order multipole radiation from quantum Hall states in Dirac materials. *Phys. Rev. B* **95**, 235439 (2017).
15. Takahashi, H. T., Proskurin, I. & Kishine, J.-i Landau level spectroscopy by optical vortex beam. *J. Phys. Soc. Jpn.* **87**, 113703 (2018).
16. Cao, B., Grass, T., Solomon, G. & Hafezi, M. Optical flux pump in the quantum Hall regime. *Phys. Rev. B* **103**, L241301 (2021).
17. Hübener, H. et al. Engineering quantum materials with chiral optical cavities. *Nat. Mater.* **20**, 438–442 (2021).
18. Suarez-Forero, D. G. et al. Spin-selective strong light–matter coupling in a 2D hole gas-microcavity system. *Nat. Photon.* **17**, 912–916 (2023).
19. Ozawa, T. et al. Topological photonics. *Rev. Mod. Phys.* **91**, 015006 (2019).
20. Lodahl, P. et al. Chiral quantum optics. *Nature* **541**, 473–480 (2017).
21. Jalali Mehrabad, M., Mittal, S. & Hafezi, M. Topological photonics: fundamental concepts, recent developments, and future directions. *Phys. Rev. A* **108**, 040101 (2023).
22. Allen, L., Barnett, S. M. & Padgett, M. J. *Optical Angular Momentum* (CRC Press, 2003).
23. Bliokh, K. Y. et al. Roadmap on structured waves. *J. Opt.* **25**, 103001 (2023).
24. Rosen, G. F. Q., Tamborenea, P. I. & Kuhn, T. Interplay between optical vortices and condensed matter. *Rev. Mod. Phys.* **94**, 035003 (2022).
25. Ji, Z. et al. Photocurrent detection of the orbital angular momentum of light. *Science* **368**, 763–767 (2020).
26. Cohen-Tannoudji, C. & Kastler, A. in *Progress in Optics* Vol. 5, 1–81 (Elsevier, 1966).
27. Cao, B. et al. Chiral transport of hot carriers in graphene in the quantum Hall regime. *ACS Nano* **16**, 18200–18209 (2022).
28. Feldman, B. E. et al. Observation of a nematic quantum Hall liquid on the surface of bismuth. *Science* **354**, 316–321 (2016).
29. Scalari, G. et al. Ultrastrong coupling of the cyclotron transition of a 2D electron gas to a THz metamaterial. *Science* **335**, 1323–1326 (2012).
30. Appugliese, F. et al. Breakdown of topological protection by cavity vacuum fields in the integer quantum Hall effect. *Science* **375**, 1030–1034 (2022).
31. Grass, T. et al. Optical control over bulk excitations in fractional quantum Hall systems. *Phys. Rev. B* **98**, 155124 (2018).
32. Knüppel, P. et al. Nonlinear optics in the fractional quantum Hall regime. *Nature* **572**, 91–94 (2019).
33. Ivanov, P. A., Letscher, F., Simon, J. & Fleischhauer, M. Adiabatic flux insertion and growing of Laughlin states of cavity Rydberg polaritons. *Phys. Rev. A* **98**, 013847 (2018).
34. Binanti, F., Goldman, N. & Repellin, C. Spectroscopy of edge and bulk collective modes in fractional Chern insulators. *Phys. Rev. Research* **6**, L012054 (2024).
35. Winter, L. & Zilberberg, O. Fractional quantum Hall edge polaritons. Preprint at https://arxiv.org/abs/2308.12146 (2023).
36. Katan, Y. T. & Podolsky, D. Modulated Floquet topological insulators. *Phys. Rev. Lett.* **110**, 016802 (2013).
37. Bhattacharya, U. et al. Fermionic Chern insulator from twisted light with linear polarization. *Phys. Rev. B* **105**, L081406 (2022).
38. Kim, H., Dehghani, H., Ahmadabadi, I., Martin, I. & Hafezi, M. Floquet vortex states induced by light carrying an orbital angular momentum. *Phys. Rev. B* **105**, L081301 (2022).
39. Bao, C., Tang, P., Sun, D. & Zhou, S. Light-induced emergent phenomena in 2D materials and topological materials. *Nat. Rev. Phys.* **4**, 33–48 (2022).
40. But, D. et al. Suppressed Auger scattering and tunable light emission of Landau-quantized massless Kane electrons. *Nat. Photon.* **13**, 783–787 (2019).
41. Zewail, A. H. Four-dimensional electron microscopy. *Science* **328**, 187–193 (2010).

Methods

Sample fabrication and preparation

Graphene was exfoliated from natural graphite crystals (HQ Graphene) and hBN was exfoliated from lab-grown[42] or commercial (HQ Graphene) synthetic crystals. A hot pickup technique was used to stack the hBN/graphene/hBN heterostructure, which was then transferred onto a pre-patterned local metallic back-gate made of 3 nm of Cr and 2 nm of Pt[43]. The area for the outer contact was etched using a selective reactive ion etching, which was followed by the evaporation of 50 nm of Au to form the outer contact[44]. Next, a third layer of hBN was dropped on top of the heterostructure to act as an insulating layer between the overlapping parts of the contacts. The same selective etch was used to expose the area for the inner contact and 100 nm of Au was evaporated to make the contact. The fabricated devices were wire-bonded to chip carriers for the electrical and PC measurements.

Measurement set-up

The sample, inside a variable temperature insert (VTI), is mounted on top of a piezoelectric stack, cooled to 4.2 K using liquid helium, and can reach magnetic fields of up to 9 T. The VTI has an optical window on top and a confocal microscope is built above to optically resolve the sample. The pump laser is illuminated through the same window and the laser spot's alignment to the sample can be monitored with the microscope. During measurements, the laser power is constantly monitored with a power meter, and feedback is given to a proportional-integral-derivative loop controlling a laser power control module. For all measurements in the main text and Supplementary Information with the exception of power dependence measurements, the average pump power is kept at 10 μW. To generate beams with OAM, a Gaussian beam is diffracted off of a phase-only SLM showing a pitchfork pattern. For PC measurements, the two sample contacts are connected to a custom-built trans-impedance amplifier (TIA) outside of the cryostat[27]. The outputs of the TIA are connected to a lock-in amplifier (SRS SR860). The pump laser is chopped at a frequency of 308 Hz and the lock-in is frequency-locked to the chopper.

Data availability

All of the data that support the findings of this study are reported in the main text, Supplementary Information and Supplementary Video 1. Source data are available from the corresponding authors on reasonable request.

References

42. Watanabe, K., Taniguchi, T. & Kanda, H. Direct-bandgap properties and evidence for ultraviolet lasing of hexagonal boron nitride single crystal. *Nat. Mater.* **3**, 404–409 (2004).
43. Pizzocchero, F. et al. The hot pick-up technique for batch assembly of van der Waals heterostructures. *Nat. Commun.* **7**, 11894 (2016).
44. Jessen, B. S. et al. Lithographic band structure engineering of graphene. *Nat. Nanotechnol.* **14**, 340–346 (2019).

Author contributions

D.S. and M.J.M. performed the experiments and analysed the data. N.P. and R.S. fabricated the graphene sample using hBN from K.W. and T.T. B.C., D.G.S.F., K.L., M.S.A. and G.S.S. contributed to building the measurement set-up and software used for measurements. B.C., M.H. and G.S.S. conceived the idea for the experiment. Theoretical analysis was performed by C.J.E., T.G. and J.S. The results were interpreted by D.S., M.J.M., N.S. and M.H. D.S., M.J.M. and M.H. wrote the paper with input from all authors.

Competing interests

The authors declare no competing interests.

Additional information

Supplementary information The online version contains supplementary material available at https://doi.org/10.1038/s41566-024-01565-1.

Correspondence and requests for materials should be addressed to Mahmoud Jalali Mehrabad or Mohammad Hafezi.

Peer review information *Nature Photonics* thanks Ido Kaminer and the other, anonymous, reviewer(s) for their contribution to the peer review of this work.

Reprints and permissions information is available at www.nature.com/reprints.

nature photonics

Optical pumping of electronic quantum Hall states with vortex light
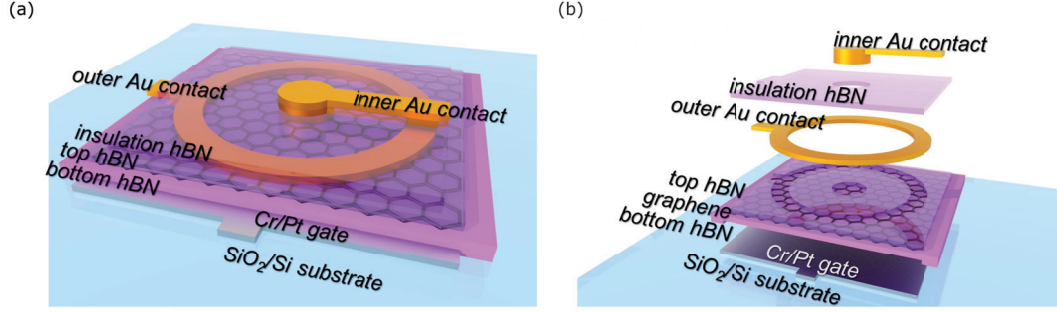
CONTENTS

FIG. S1.   Sample fabrication: (a) Schematic of the graphene Corbino sample. (b) Exploded view of (a).

S1. DEVICE FABRICATION

Graphene was exfoliated from natural graphite crystals (HQ Graphene) and hBN was exfoliated from lab-grown [1] or commercial (HQ Graphene) synthetic crystals. Monolayer graphene and hBN were identified based on their color contrast with an optical microscope, while the thickness of the hBN layers used as a gate insulator was measured by atomic force microscopy. A hot pickup technique was used to stack the hBN/graphene/hBN heterostructure, which was then transferred onto a pre-patterned local metallic back-gate made of 3 nm of Cr and 2 nm of Pt [2]. The area for the outer contact was etched using a selective reactive ion etching which was followed by the evaporation of 50 nm of Au to form the outer contact [3]. Next, a third layer of hBN was dropped on top of the heterostructure to act as an insulating layer between the overlapping parts of the contacts. The same selective etch was used to expose the area for the inner contact and 100 nm of Au was evaporated to make the contact. The fabricated devices were wire-bonded to chip carriers for the electrical and photocurrent (PC) measurements.
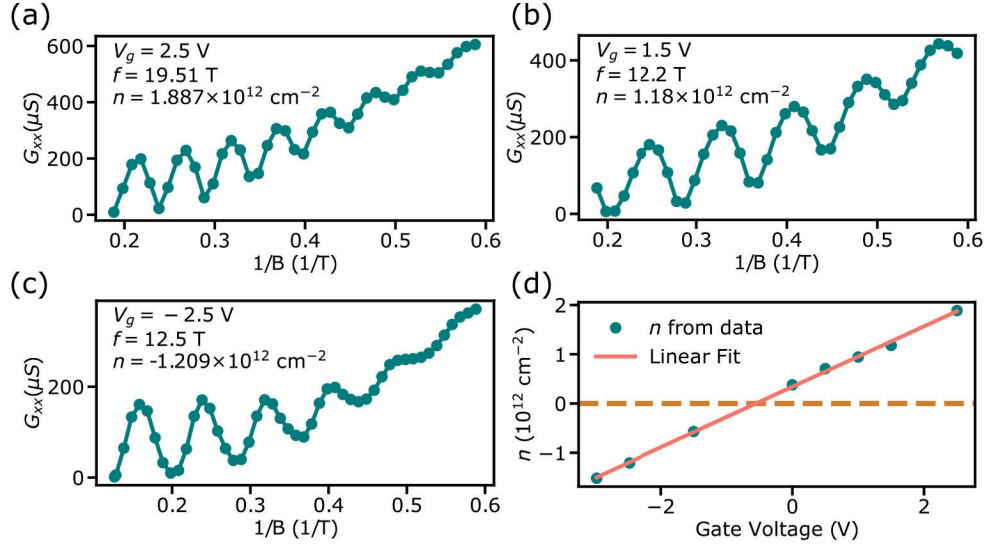
FIG. S2. Shubnikov-de Haas oscillation measurement: Longitudinal conductance measured as a function of $1/B$ at gate voltages: (a) 2.5 V, (b), 1.5 V, and (c) -2.5 V. Using a Fourier transform to extract the frequency, the carrier densities were calculated to be (a) 1.887×10^{12} cm^{-2}, (b) 1.18×10^{12} cm^{-2}, and (c) -1.209×10^{12} cm^{-2}. (d) A linear fit to the extracted carrier densities as a function of gate voltage. The slope of the least-squares linear fit is $(0.614 \pm 0.009) \times 10^{12}$ cm^{-2}V^{-1} and the y-intercept is $(0.34 \pm 0.02) \times 10^{12}$ cm^{-2}.

S2. TRANSPORT MEASUREMENTS

Transport measurements are carried out with low-frequency lock-in techniques either by biasing with a current of 20 nA or with a voltage at a frequency of 13 Hz. Gate voltage sweeping is performed using a DC source measure unit (Keithley 2450). The two-terminal longitudinal conductance for various magnetic fields was measured to obtain the Landau fan (Fig. 4c in the main text). These measurements are performed using the circuits depicted in Fig. S3a-b.

To calibrate the conversion between gate voltage and carrier density, we measured Shubnikov-de Haas oscillations by setting the gate voltage and sweeping the magnetic field. The carrier density is extracted from the frequency of the oscillation (f) by $n = 4ef/h$ [4]. We extracted the carrier density for gate voltages between -3 V and 2.5 V and used a linear fit as a conversion between gate voltage and carrier density, see Fig. S2.
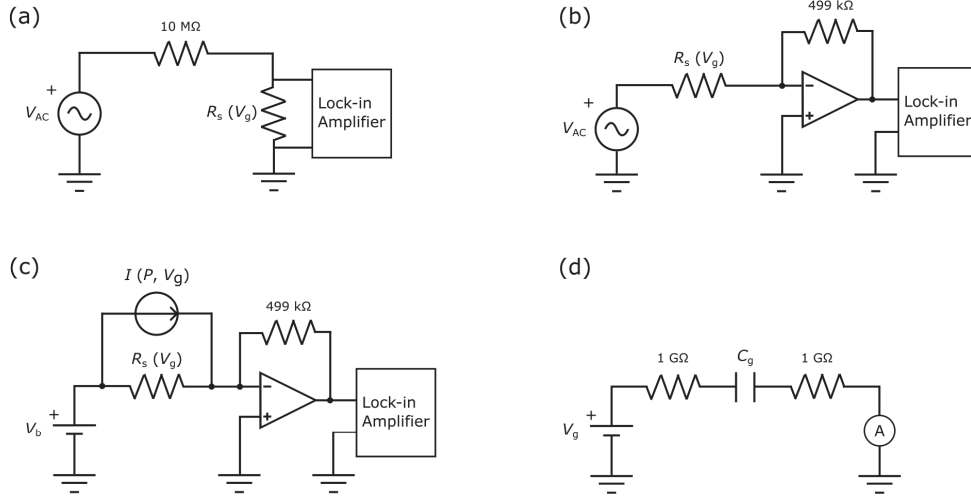
FIG. S3. Experimental setup: (a) The current bias circuit used for transport measurements. A sinusoidal voltage is provided by the lock-in amplifier. The constant resistor (10 MΩ) is in series with the sample R_{S}. This large resistor is used to current bias the sample. The voltage across the sample is measured through the inputs of the lock-in amplifier. (b) The voltage bias circuit is alternatively used for transport measurements. We use the same source as in (a), however, there is no large resistor to convert the voltage signal to current. In this case, the resulting current from the sample is passed through a trans-impedance amplifier (TIA), and the resulting voltage is measured with the lock-in amplifier. (c) The effective circuit for measuring PC. In this circuit, the sample is modeled as a current source, I (P, V_{g}), in parallel with a resistor (sample resistance). The sample is in series with a DC voltage source. The TIA is in series with the sample and is connected to both terminals of the lock-in amplifier. (d) The effective circuit used to gate the sample: in this circuit, the sample is treated as a capacitor with capacitance C_{g}. It is in series with two 1 GΩ resistors to decrease the current in the circuit.

S3. PC MEASUREMENTS

The sample, inside a variable temperature insert (VTI), is mounted on top of a piezo-electric stack (scanners (ANSxy100) and positioners (ANPx101, ANPz201)). It is cooled down to 4.2 K using liquid helium and can reach magnetic fields up to 9 T. The VTI has an optical window on top and a confocal microscope is built above to optically resolve the sample. This includes an aspheric lens (Thorlabs C330TMD - B) with a numerical aperture (NA) of 0.68 and a focal length of 3.10 mm mounted above the sample. The pump laser is illuminated through the same window and the laser spot's alignment to the sample can be monitored with the microscope. During measurements, the laser power is constantly monitored with a power meter right before the beam enters the optical window, and a feedback is given to a proportional-integral-derivative loop controlling a laser power control module. The power control module consists of a DC voltage applied to a Thorlabs electronic variable optical attenuator. For all measurements in the main text and SI with the exception of power dependence measurements, the average pump power is kept at 10 μW. Laser illumination at such a low pump power is unlikely to significantly impact quantum Hall physics. This is also
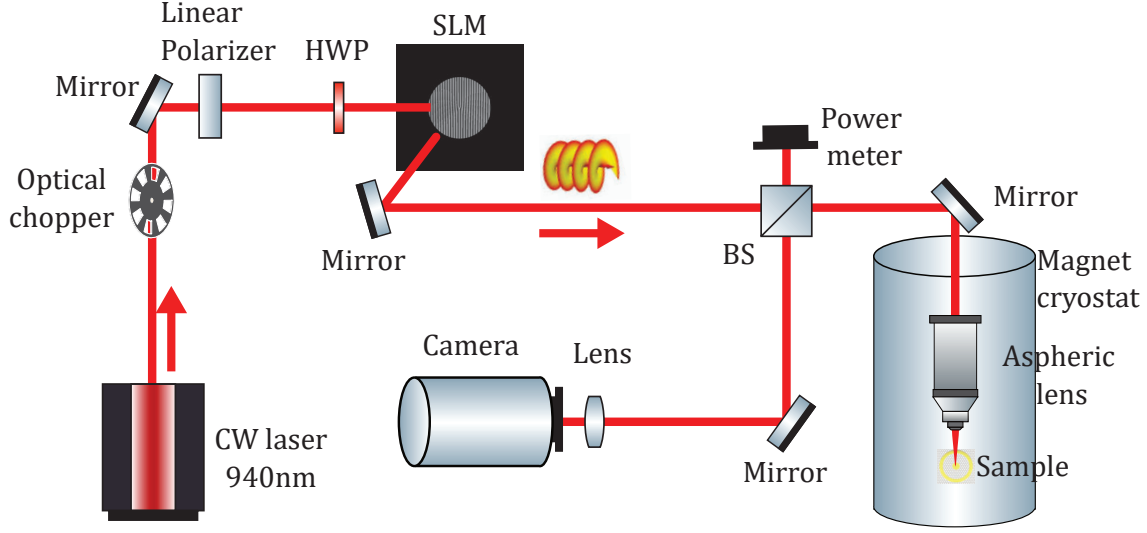
FIG. S4. The optical setup used for the PC generation.

evidenced by previous works, where in an experiment in a rectangular graphene sample where quantum Hall edge physics was investigated with photocurrent measurements, it was found that optical illumination (with pump power comparable to our case of a few μW) did not impact the quantum Hall physics [5]. This indicates that the sample does not heat up enough for it to change its properties.

The two sample contacts are connected to a custom-built trans-impedance amplifier (TIA) outside of the cryostat [5]. The outputs of the TIA are connected to a lock-in amplifier (SRS SR860). The pump laser is chopped at a frequency of 308 Hz and the lock-in is frequency-locked to the chopper.

We sweep the gate in the same way as in the transport measurement. However, in the PC measurements, we apply a DC voltage bias across the sample using an SRS SIM928. The PC measurements are performed using the circuit depicted in Fig. S3c and the optical setup depicted in Fig. S4.
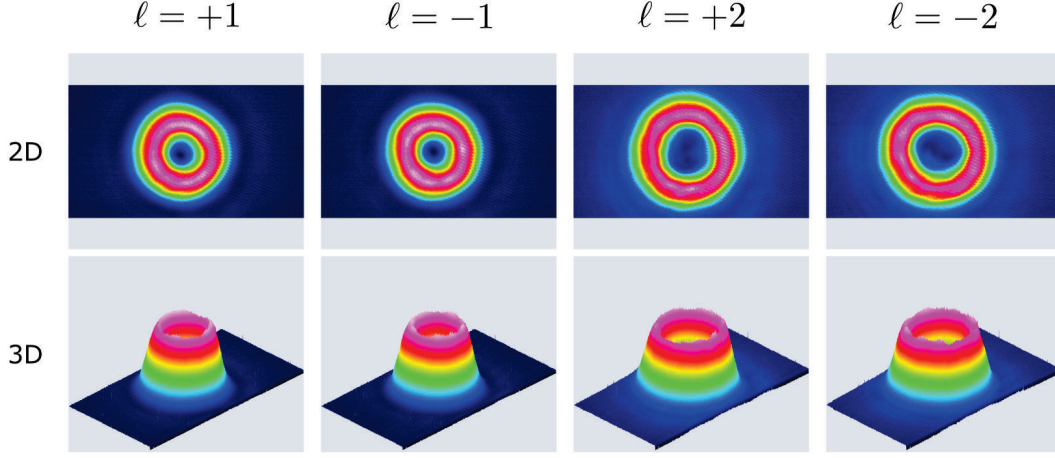
FIG. S5.   Beam profiles are imaged with a beam profiler for $\ell = +1$, $\ell = -1$, $\ell = +2$, and $\ell = -2$. Images are taken of the collimated beam diverted from the sample path.

S4. GENERATION AND OPTIMIZATION OF ORBITAL ANGULAR MOMENTUM BEAMS

To generate beams with orbital angular momentum (OAM) a Gaussian beam is diffracted off of a phase-only spatial light modulator (SLM). Ideally, the pattern displayed to achieve this would be

$$h(r,\theta) = \frac{1}{2\pi}\mathrm{mod}\left(\ell\theta - \frac{2\pi}{\mathrm{D}}\mathrm{r}\cos(\theta),\ 2\pi\right). \tag{S1}$$

This blazed hologram maximizes the diffraction efficiency [6, 7]. The obtained diffraction modes are a superposition of Laguerre-Gaussian (LG) modes with the same ℓ but various p which is the transverse index of the LG mode [8]. A Meadowlark optics 1920x1152 XY Phase series SLM is used. The performance of the pixels in the SLM is not homogeneous. The phase hologram can be modified to compensate for this. The phase hologram used in the experiment is

$$h(r,\theta) = \mathcal{M}(r,\theta)\mathrm{mod}\left(\mathcal{F}(\mathrm{r},\theta) + \frac{2\pi}{\mathrm{D}}\mathrm{r}\cos(\theta),\ 2\pi\right), \tag{S2}$$

where $\mathcal{M} = 1 + \frac{1}{\pi}\mathrm{sinc}^{-1}(\mathrm{A}(\mathrm{r},\theta))$ and $\mathcal{F} = \Phi - \pi\mathcal{M}$. The beam can be optimized by setting $\Phi = \ell\theta$ and manually adjusting the function $A(r,\theta)$ until a satisfactory beam is reached [9, 10]. The OAM beams after optimization are shown in Fig. S5.

To verify that the beams used in the experiment have the correct OAM, the beam's reflection off of the sample was interfered with a Gaussian reference beam. The results can be seen in Fig. S6. The interference patterns show the same pitchfork but in opposite directions, verifying that one has $\ell = +1$ and the other has $\ell = -1$.

S4a. Profile Intensity Comparison

To minimize the beam profile intensity mismatch effects in the PC measurements, beam optimization was performed to make the beams with opposite OAMs as similar as possible. However, naturally, the beams will not be perfectly identical, as can be seen in Fig. S5. This is important since differing beam profiles can cause a difference in generated PC. To quantify and demonstrate the insignificance of this effect in our experiments, the overlap of the beams is calculated using the following function:

$$O[I(x,y), J(x,y)] = \frac{\left| \int \int I(x,y)J(x,y)dxdy \right|^2}{\int \int |I(x,y)|^2 \, dxdy \int \int |J(x,y)|^2 \, dxdy}, \tag{S3}$$

where $I(x,y)$ and $J(x,y)$ are the two beam profiles with opposite OAMs. The maximum possible overlap is one. The calculated overlap for the $\ell = \pm 1$ and $\ell = \pm 2$ beams is 0.96 and 0.92 respectively. In other words, the $\ell = \pm 1$ beams have a 4% difference and the $\ell = \pm 2$ beams have an 8% intensity profile difference. The minimum percent difference between the average total current and the subtracted current for $\ell = \pm 2$ at $B = 9$ T is 60%. For $B = -9$ T it is 134%. For $\ell = \pm 1$ the minimum percent differences are 78% and 75% respectively. This confirms that the beam profiles' intensity mismatch cannot be affecting our observations.

Moreover, the beam profiles do not change with flipping the magnetic field, further confirming that the intensity profile mismatch cannot cause the sign of the PC difference to flip for the opposite magnetic field.

Here we note that making the $\ell = \pm 1$ and $\ell = \pm 2$ beams spatially comparable in size can be helpful in our experiment, specifically for the comparison of the photocurrent generated with beams carrying different OAM quantum numbers. A possible method may be to defocus the $\ell = \pm 1$ beam and increase its spatial profile. However, it is important to note that defocusing the beam may introduce further non-paraxial complexities which can make drawing comparisons between photocurrent generated with beams with different OAM quantum numbers not immediately conclusive. In particular, one complexity can be the possible mixing of SAM-OAM degrees of freedom which in the main text we studied in detail for the case of perfectly focused beams in the polarization-dependence section. Such SAM-OAM mixing may introduce a defocusing-dependant modification to the OAM's role in the generated radial PC, which in turn weakens the strength of such potential comparative conclusions drawn from the measured PC signals generated by OAM beams with different focusing. Therefore, rigorous investigation of the OAM-number dependence of the radial photocurrent remains an intriguing avenue to explore.
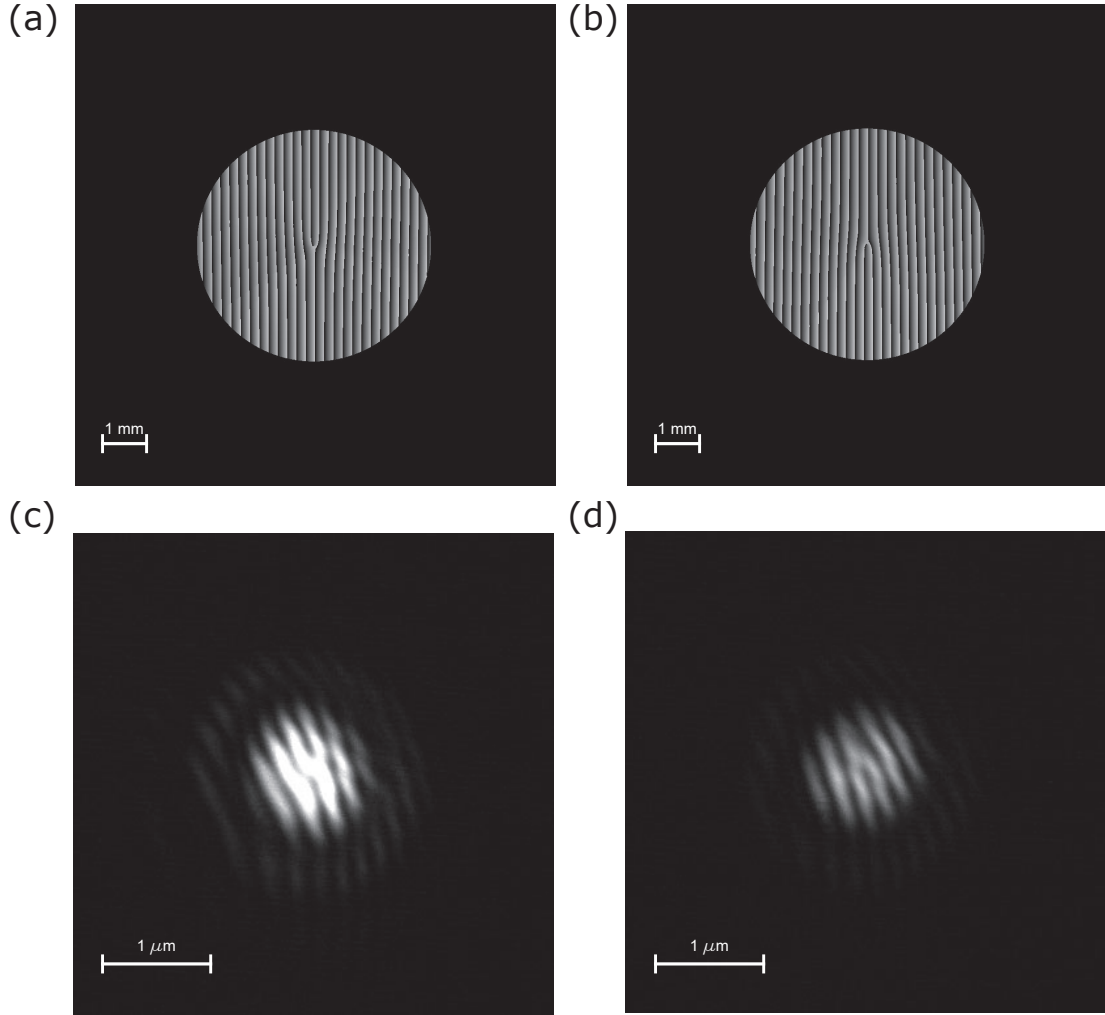
FIG. S6. (a) Grating displayed on SLM to generate $\ell = +1$ as the first diffraction order. (b) The same as (a), but for $\ell = -1$. (c) Interference pattern when the $\ell = +1$ beam interferes with a Gaussian beam on the sample substrate. (d) The same as (c), but with $\ell = -1$.

S5. GATE VOLTAGE SWEEP MEASUREMENTS FOR DIFFERENT BIAS

The gate voltage dependence for different bias voltages was also measured. It is observed that the gate voltage dependence changes very little with bias voltage and the flip with magnetic field stays the same.

FIG. S7. Measured PC difference as a function of gate voltage for different V_b at $B = 9$ T: (a) Subtraction of PC for $\ell = \pm 1$. (b) Subtraction of PC for $\ell = \pm 2$.

S6. REFLECTION IMAGING OF THE SAMPLE

In the PC measurement setup depicted in Fig. S4, it is difficult to obtain a high enough quality image of the sample to properly align the beam to it. Another method is to use a Gaussian beam, the same used for PC me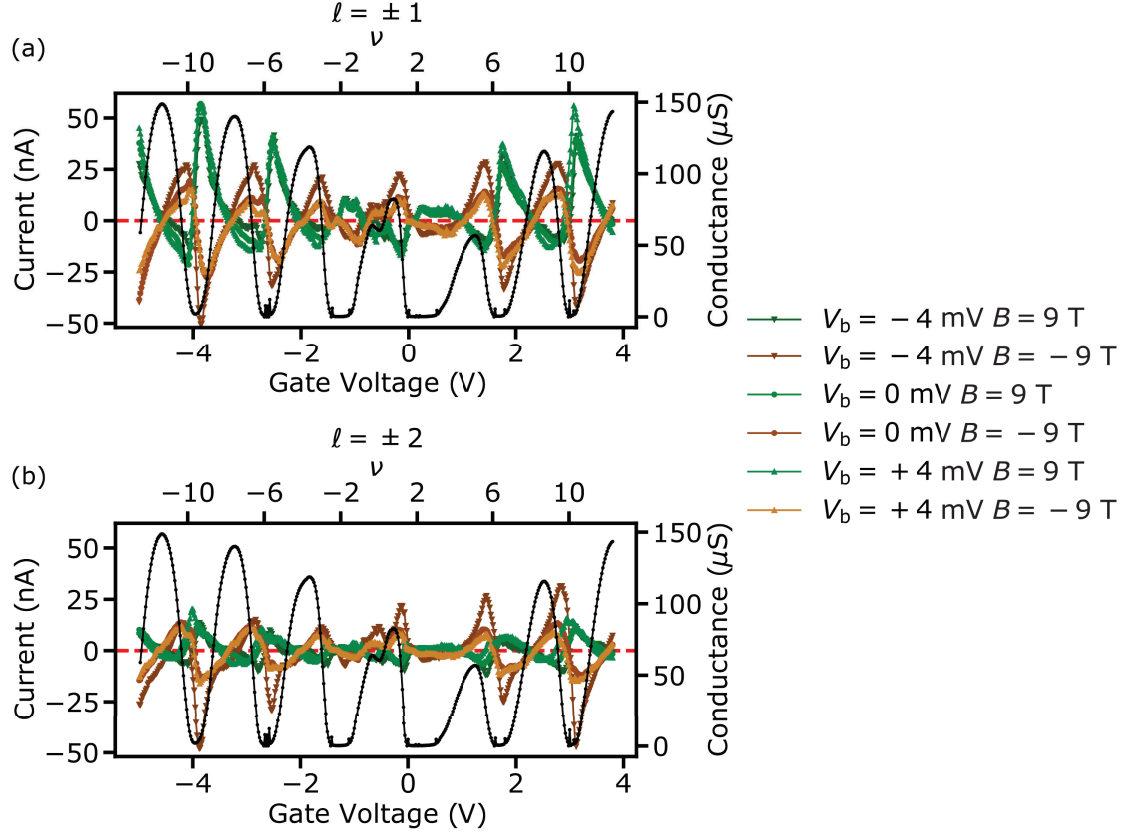asurements with $\ell = 0$, and move the sample using scanners (ANSxy100) while collecting the reflection with a photodiode. The measured voltage from the photodiode can be used to make an image of the sample; one of these images is shown in Fig. S8b. The gold contacts on the sample are highly reflective in comparison to the hBN/graphene/hBN heterostructure, therefore, in the image, the gold contacts will appear bright and areas of the sample without gold will appear dark (with the chosen color map). Since the outer boundary of the Corbino sample is covered with a gold contact and the center of the Corbino also has a gold contact, the image clearly defines the boundaries of the sample which can then be used for beam alignment.
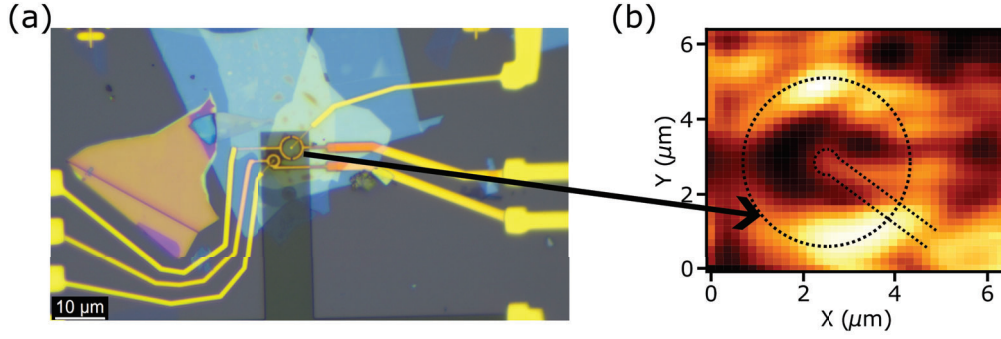

FIG. S8. (a) Image of the sample taken with an optical microscope. (b) Image of the sample taken by measuring the optical reflection of the pump beam with a photodiode while moving the sample with scanners. The dashed curves show the outline of the Corbino sample.

S7. SELECTION RULES

We discuss the selection rules of exciting electrons with light from the lower to the upper band in graphene in the Quantum Hall regime, considering the possibility that the light might carry non-zero OAM. We consider the electromagnetic vector potential $\vec{A}$ of incident light coupled via Peierls substitution $\vec{k} \to \vec{k} - e\vec{A}$ and compute transition matrix elements as

$$M(n_{\rm f}, m_{\rm f}, n_{\rm i}, m_{\rm i}) = -e v_{\rm F} \langle n_{\rm f}, m_{\rm f} | \vec{A}(\vec{r}) \cdot \vec{\sigma} | n_{\rm i}, m_{\rm i} \rangle \tag{S4}$$

where $|n_{\rm x}, m_{\rm x}\rangle$ denotes initial (x = i) and final (x = f) states. $n_{\rm x}$ denotes the LL and $m_{\rm x}$ the quantum number related to angular momentum. The expected angular momentum in z-direction can be computed as $\langle L_z \rangle = \hbar(m-n)$. We compute the matrix elements in the spinor representation of the wave-function limiting to transitions from the lower band of graphene (negative n) to the upper band (positive n) and assuming $n \neq 0$. For σ^+ polarized light, $\vec{A}(\vec{r}) \cdot \vec{\sigma} = A(\vec{r})\sigma^+$, we get

$$M^+(n_{\rm f}, m_{\rm f}, n_{\rm i}, m_{\rm i}) = -\frac{e v_{\rm F}}{2} \left(\langle n_{\rm f} - 1, m_{\rm f} |, \ \langle n_{\rm f}, m_{\rm f} | \right) A(\vec{r})\sigma^+ \begin{pmatrix} |n_{\rm i} - 1, m_{\rm i}\rangle \\ -|n_{\rm i}, m_{\rm i}\rangle \end{pmatrix}$$
$$= \frac{e v_{\rm F}}{2} \langle n_{\rm f} - 1, m_{\rm f} | A(\vec{r}) | n_{\rm i}, m_{\rm i} \rangle \tag{S5}$$

while for σ^- polarized light we get

$$M^-(n_{\rm f}, m_{\rm f}, n_{\rm i}, m_{\rm i}) = -\frac{e v_{\rm F}}{2} \langle n_{\rm f}, m_{\rm f} | A(\vec{r}) | n_{\rm i} - 1, m_{\rm i} \rangle. \tag{S6}$$
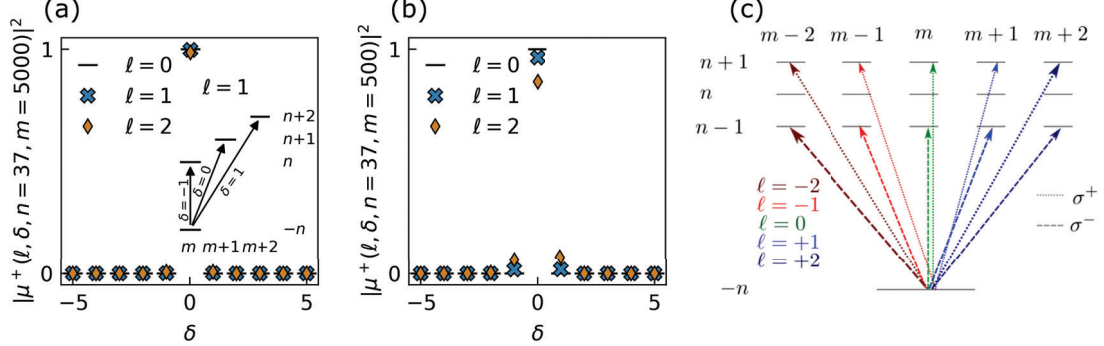

FIG. S9. (a) Matrix element $\mu^+(\ell, \delta, n, m)$ as defined in Eq. (S10) as a function of δ for $\ell = 0, 1, 2$ as in the experiment (limiting to positive OAM). $n = 37$ is fixed as in the experiment and $m = 5000$ which corresponds to a state with expected radial position $\langle r \rangle_{n=37, m=5000} \approx 1 \ \mu$m which is somewhere in the middle of the sample, with radius $R = 2 \ \mu$m. The inset illustrates the effect of δ in the case of $\ell = 1$: $\delta = 0$ corresponds to the situation where the OAM of the light only changes the quantum-number m while $\delta \neq 0$ considers further transitions where n and m are simultaneously changed. Only the $\delta = 0$ transition has substantial weight. (b) Same as in (a) just with $m = 500$ which corresponds to a radial position of the electron of $\langle r \rangle_{n=37, m=500} \approx 300$ nm hence close to the inner contact. The $\delta = 0$ transitions also dominate here but for smaller m, $\delta \neq 0$ transitions have an increased weight. (c) Illustration of selection rules considering only $\delta = 0$ that have the dominant weight (see (a) and (b)).

For light carrying OAM, we write $A(\vec{r}) = Ae^{i\varphi\ell}$, $\ell = 0, \pm 1, \pm 2, \ldots$ assuming no radial dependence of the light field. We compute the dimensionless and normalized matrix elements for σ^+ polarized light

$$\mu^+ = \langle n_{\mathrm{f}} - 1, m_{\mathrm{f}} | e^{i\varphi\ell} | n_{\mathrm{i}}, m_{\mathrm{i}} \rangle \tag{S7}$$

and σ^- polarized light

$$\mu^- = \langle n_{\mathrm{f}}, m_{\mathrm{f}} | e^{i\varphi\ell} | n_{\mathrm{i}} - 1, m_{\mathrm{i}} \rangle \tag{S8}$$

using the wave-functions

$$\langle r, \varphi | n, m \rangle = \frac{i^{(m-n)}}{\sqrt{2\pi}\ell_{\mathrm{B}}} \sqrt{\frac{n!}{m!}} e^{-\frac{r^2}{4\ell_{\mathrm{B}}^2}} e^{i\varphi(m-n)} r^{(m-n)} L_n^{(m-n)} \left(\frac{r^2}{2\ell_{\mathrm{B}}^2} \right). \tag{S9}$$

Here $L_a^b(x)$ are the associated Laguerre polynomials. We assume $n < m - 1$, since this is the relevant case for the experiment. In what follows, we will focus on σ^+ polarized light computing μ^+. However, analogous steps can be performed to compute the matrix elements μ^-. Inserting the wave function [11, 12] Eq. (S9) into Eq. (S7) we get

$$\mu^+ = i^{(m_{\mathrm{i}} - m_{\mathrm{f}} - n_{\mathrm{i}} + n_{\mathrm{f}} - 1)} \sqrt{\frac{n_{\mathrm{i}}!(n_{\mathrm{f}} - 1)!}{m_{\mathrm{i}}!m_{\mathrm{f}}!}} \frac{1}{2\pi} \int_0^{2\pi} \mathrm{d}\varphi \, e^{i\varphi(m_{\mathrm{i}} - m_{\mathrm{f}} - n_{\mathrm{i}} + n_{\mathrm{f}} - 1 + \ell)}$$
$$\int_0^\infty \mathrm{d}x \, 2xe^{-x^2} x^{m_{\mathrm{i}} + m_{\mathrm{f}} - n_{\mathrm{i}} - n_{\mathrm{f}} + 1} L_{n_{\mathrm{i}}}^{m_{\mathrm{i}} - n_{\mathrm{i}}}(x^2) L_{n_{\mathrm{f}} - 1}^{m_{\mathrm{f}} - n_{\mathrm{f}} + 1}(x^2). \tag{S10}$$

The angular integral enforces angular momentum conservation. We introduce $n := n_i$ and $m := m_i$ and define

$$\begin{aligned} n_{\mathrm{f}} &=: n + \delta + 1 \\ m_{\mathrm{f}} &=: m + \ell + \delta \end{aligned} \tag{S11}$$

such that angular momentum conservation is fulfilled for any choice of n, m, ℓ, and δ. Note that Refs. [5, 13] only considered $\delta = 0$ case. With this

$$\mu^+(\ell, \delta, n, m) = i^\ell \sqrt{\frac{n!(n+\delta)!}{m!(m+\delta+\ell)!}} \int_0^\infty \mathrm{d}x \, 2xe^{-x^2} x^{2(m-n)+\ell} L_n^{m-n}(x^2) L_{n+\delta}^{m-n+\ell}(x^2). \tag{S12}$$

We plot μ^+ as a function of δ for $\ell = 0, +1, +2$ in Fig. S9 for $n = 37$ and $m = 5000$ (a) and $m = 500$ (b). For $m = 5000$ the expected radial position of the electron is $\langle r \rangle_{n=37,m=5000} \approx 1 \ \mu$m hence somewhat in the radial middle of the sample that has an overall radius of $R \approx 2 \ \mu$m. For $m = 500$ we have $\langle r \rangle_{n=37,m=500} \approx 300$ nm, which is close to the radius of the inner contact. For $\ell = 0$ the orthogonality of the Laguerre polynomials enforces $\delta = 0$ such that we get the well known selection rules [12]

$$\mu^+(\ell = 0, \delta, n, m) = \delta_{\delta,0} \Rightarrow \mu^+ = \delta_{n_{\mathrm{f}} - 1, n_{\mathrm{i}}} \delta_{m_{\mathrm{f}}, m_{\mathrm{i}}} \tag{S13}$$

and for μ^-

$$\mu^-(\ell = 0, \delta, n, m) = \delta_{\delta,0} \Rightarrow \mu^- = \delta_{n_{\mathrm{f}}, n_{\mathrm{i}} - 1} \delta_{m_{\mathrm{f}}, m_{\mathrm{i}}}. \tag{S14}$$

For $\ell \neq 0$ we don't get strict Kronecker-Delta-like selection rules but instead, multiple transitions are in principle allowed. However, as can be seen in Fig. S9, transitions with $\delta \neq 0$ are suppressed compared to the $\delta = 0$ transitions. We illustrate the selection rules, only considering $\delta = 0$, in Fig. S9 (c).

Importantly from the selection rules described above, we can see that polarization should not generate a radial photocurrent. This is due to the fact that the polarization only changes n and not m. Although the radius of the electronic wavefunction depends on both n and m, when the electron is excited, n will increase according to the selection rules, but will then relax to a lower value depending on the placement of E_{F}. In contrast, m will continue to change by ℓ each time the electron is cyclically excited. This results in the electronic wavefunction, depending on the sign of ℓ, to either expand or contract each time it is excited by light with $\ell \neq 0$. The relationship between the expected radius and n and m is described in the next section.

In the main text, as a control experiment, we have inverted the B-field $\vec{B} \to -\vec{B}$. It is therefore interesting to consider how the selection rules change in this case. For deriving the selection rules as above, we have used the B-field to define the z-axis of the system. Therefore the sign of the OAM of light as well as the handedness of the polarization is determined by whether they are aligned or anti-aligned with the magnetic field. Inverting the B-field is therefore equivalent to inverting the OAM and the polarization. Hence we can relate the transition matrix elements at magnetic field $\vec{B}$ and $-\vec{B}$ as

$$\mu^+(\ell, \delta, n, m)\Big|_{\vec{B}} = \mu^-(-\ell, \delta, n, m)\Big|_{-\vec{B}}. \tag{S15}$$

Based on this observation, when measuring the subtracted photo-current at magnetic field $\vec{B}$

$$\Delta I\Big|_{\vec{B}} = I^{+\ell}\Big|_{\vec{B}} - I^{-\ell}\Big|_{\vec{B}} \tag{S16}$$

one expects this to change sign when inverting the magnetic field hence

$$\Delta I\Big|_{\vec{B}} = -\Delta I\Big|_{-\vec{B}}. \tag{S17}$$

This is what we have used as a control experiment in the main text and indeed we observe the same sign reversal in the experiment.

S8. RELATION BETWEEN EXPECTED RADIUS AND QUANTUM NUMBERS n AND m

In this part, we compute the expected radius of the electronic wavefunctions in graphene in the quantum Hall regime. In spinor representation, they can be computed as

$$
\langle r \rangle = \begin{cases} \langle n = 0, m | r | n = 0, m \rangle; & n = 0 \\ \frac{1}{2} \left(\langle n, m | r | n, m \rangle + \langle n - 1, m | r | n - 1, m \rangle \right); & n \neq 0 \end{cases} \quad . \tag{S18}
$$

The wave functions $\phi_{n,m}(r) = \langle r, \phi | n, m \rangle$ read [11, 12]

$$
\phi_{n,m}(r, \varphi) = \frac{i^{|n-m|}}{\sqrt{2\pi}\ell_B} \sqrt{\frac{\min(n,m)!}{\max(n,m)!}} e^{-\frac{r^2}{4\ell_B^2}} e^{i\varphi|n-m|} r^{|n-m|} L_{\min(n,m)}^{|n-m|}\left(\frac{r^2}{2\ell_B}\right) \tag{S19}
$$

and are normalized according to

$$
\int_{\mathbb{R}^2} d\vec{r}\, \phi_{n,m}(\vec{r}) \phi_{n',m'}^*(\vec{r}) = \delta_{n,n'}\delta_{m,m'}. \tag{S20}
$$

We show the expected radii as a function of the quantum number m for different values of n in Fig. S10. For $n = 0$ the expected position approximately coincides with the position of the guiding center $r_{\text{Guide}} = \ell_B\sqrt{2m+1}$ while for larger n one gets larger radii as expected.
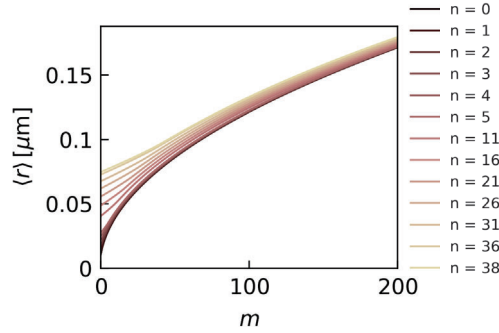

FIG. S10. Expected radial position $\langle r \rangle$ according to Eq. (S18) as a function of quantum number m in different LLs n.

S9. IDEAL INTERACTING QUANTUM HALL OAM RESPONSE

The above argument can be generalized to understand the OAM PC in the presence of Coulomb interactions. Let us consider photons incident on disorder-free Graphene in a perfect Corbino geometry with a magnetic field and Coulomb interactions. The Coulomb interaction is key to helping the carriers to thermalize and our discussion includes relaxation processes such as Auger. Let us further assume that the bulk is gapped and there are two edges, i.e., an inner and outer edge, which for now we will assume to be isolated from contacts.

Given the circular symmetry, the angular momentum is the key quantum number to think about. In fact, in this ideal situation, energy E and angular momentum L are the only two conserved quantities. For a gapped bulk, the system thermalizes to a state with a low density of bulk quasi-particles. This means that the edge charge Q is also a conserved quantity. As a consequence, the final state (after the absorption of some number of photons) is characterized by edges with quantum numbers L, E, and Q.

The edge theory is more conventionally described in terms of momentum k rather than angular momentum. Note that in a magnetic field, momentum is shifted by the vector potential at radius R of the edge is $k_{\mathrm{F}} = A = BR/2$. Transferring charge Q to the edge changes momentum by Qk_{F}. Adding energy through particle-hole excitations changes momentum by E/v where v is the edge velocity. The change in angular momentum is $L = R(Qk_{\mathrm{F}} + E/v) = R(QBR/2 + E/v)$. This is consistent with the wave-functions of LLs at angular momentum m seen in the last section being at a radius $\sim \sqrt{2m/B}$.

Photons supply both OAM angular momentum l and energy E_{ph}. Considering angular momentum and ignoring the contribution of the photon energy, the total charge transferred is $\delta Q_L = 2N_{\mathrm{ph}}l/BR^2 = 2N_{\mathrm{ph}}l(l_B/R)^2$. The photon energy contribution turns out to be independent of OAM and therefore even in magnetic field. The charge transfer expression matches that from the LL wave-function picture in the previous section and shows that interactions (at least in the absence of phonons and disorder) do not affect the OAM PC, which is a result of angular momentum pumping.

S10. PC SIGN OSCILLATION: LLS AND INJECTION CURRENT PICTURE

LLs picture: As described in a simplified picture earlier (Fig. 1 main text), in the quantum Hall regime, light with non-zero OAM can induce optical transitions between the LLs such that the spatial extent of these states depends on the associated angular quantum number m, where the radius of LLs increases with m. In our Corbino device, depending on the helicity of light, this spatial expansion (shrinking) of the carriers' wavefunction manifests itself as an outward or inward radial current.

This intuitive picture for the PC generation due to the radial modulation of the electron wavefunction caused by the optical vortex does not immediately suggest PC oscillations as a function of gate voltage (V_g), which are seen in Fig. 4 of the main text. To understand this effect, one must note that the PC is actually the result of optical excitation and subsequent carrier relaxation. As known from earlier studies [5, 14] the position of E_F within a LL, controlled by V_g, gives rise to a relaxation bottleneck for either electrons or holes. Due to the opposite charges of the different carriers (electrons and holes), this leads to a change of PC polarity. That is, PC oscillations upon sweeping through a LL. While in the rectangular geometry experiment of Ref.[5] this bottleneck argument relied on equal chirality of electrons and holes at the edge of the sample, in the present scenario, the direction of transport is determined by the relative helicity of twisted light and magnetic field. Naively, one might expect that the OAM would lead to a relative shift of electron and hole position, i.e., to opposite shifts for the two types of carriers. However, Coulomb attraction ensures that the shift is experienced by the center of mass of the electron-hole-pair (see also Ref. [15] for the case of excitons). Hence, electrons and holes are moved in the same direction which explains the observed current oscillations.

Unfortunately, formalizing this picture, i.e., via optical Bloch equations as has been done in Ref. [5], is extremely complicated. Not only would it be necessary to explicitly account for LL and orbital degrees of freedom, but the picture also suggests that properly accounting for the Coulomb attraction between electrons and holes will be crucial to capture the oscillations. However, an alternative description is able to provide a formalism which is suited to explain the observed behavior.

Injection current picture: In our system, since the photon frequency is in the optical regime (pump wavelength 940 nm = 1.32 eV and $E_{n=37} - E_{n=-36} = 1.315$ eV), one expects the LL spacing ($E_{n=37} - E_{n=36} = 9$ meV) to be much smaller than the lifetime broadening of excited electrons and holes. Therefore, we can consider optically excited electrons and holes as approximately free Dirac particles. Beyond the dipole approximation, the OAM of the pump photons locally imparts momentum to the electrons and holes in the tangential direction (in the polar coordinates of the Corbino disk). Moreover, the Lorentz force from the external out-of-plane magnetic field imparts radial components to the velocity of the electron and holes. As detailed in the following section, the radial current of both the electrons and holes in this scenario is therefore given by the following

$$I_{\text{radial}} = -\frac{Bq}{k^4}\cos(2\theta)(\tau_e + \tau_h) \tag{S21}$$

where B is the external out-of-plane magnetic field, q is the local OAM-induced momentum, θ is the angle between the electron and hole's momentum k, and τ_e and τ_h are the scattering times of the electrons and holes, respectively. From the Dirac equation $k = \omega/(2v_D)$. The total induced
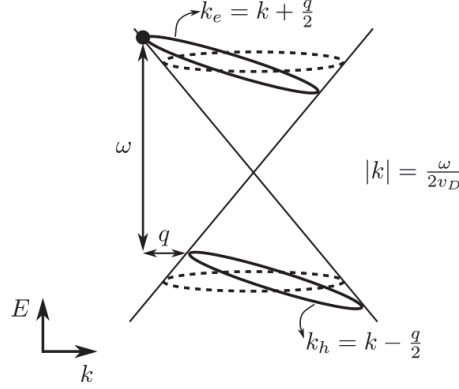
FIG. S11. Optical excitation by finite wave-vector light in a band structure of Dirac electrons in graphene.

current is

$$I_{\text{meas}} = \int d\theta W(\theta) I_{\text{radial}}(\theta) \tag{S22}$$

where $W(\theta)$ is the weight of the current contribution from the electrons and holes moving at the angle θ. In an ideal case, W should be θ-independent, leading to a vanishing of the measured current in our system. However, as explained later in the following section, W can be a function of both θ and the longitudinal conductivity, which is a function of the carrier density (and therefore gate voltage V_{g}) and B. This can potentially explain the observed V_{g}-dependent polarity change of the measured PC.

S11. THEORY OF OAM PHOTORESPONSE IN THE STRONG SCATTERING REGIME

The OAM field from light with frequency ω can be written as $A(\vec{r}) \propto e^{il\theta}$, where (r, θ) are the radial and angular coordinates. This can then be expanded in terms of a tangential coordinate $x_t = r\theta$ as $A(\vec{r}) \propto e^{ilx_t/r} = e^{iqx_t}$ where $q = l/r$. Locally, in the Corbino geometry, we can approximate the OAM as a plane wave with wave-vector q.

Considering the absorption of the photon by Dirac electrons, at rate R per unit area, shown in Fig. S11, leads to an electron-hole pair with momenta $k_e = k + q/2$ and $-k_h = -(k - q/2)$, respectively, where $|k| = \omega/2v_{\text{D}}$ is independent of q. To check that this is correct note that the energy of such a pair is $|k + q/2| + |k - q/2| = 2|k| + o(q^2)$.

Next, we consider (seen in Fig. S12) the generated electron-hole pair in momentum space along with the velocity of each particle as well as the Lorentz-force induced momentum change. For a quasiparticle at momentum k (note that we designate holes to be at the momentum of the missing electron), the velocity is $u_{\text{e,h}}(k) = \pm v_{\text{D}}\vec{k}/k$. The Lorentz-force induced momentum change is $B \times u_{\text{e,h}}(k)\delta\tau_{\text{e,h}}$ where τ_{e} (τ_{h}) is the scattering time of electrons (holes). The average (over a scattering time) change in velocity induced by the Lorentz force turns out to be $\delta u_{\text{e,h}}(k) = v_{\text{D}}^2\tau_{\text{e,h}}\frac{B \times \vec{k}}{2k^2}$, which is the same for electrons and holes. The sign is independent of electrons or holes because both the velocity as well as the momentum change changes sign for both electrons or holes.
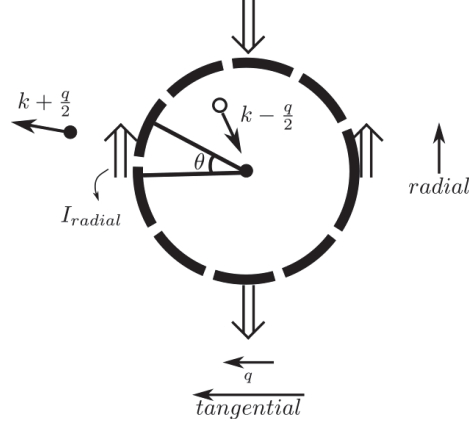
FIG. S12. Wave-vector and velocity structure of electron-hole pairs in a magnetic field excited by light at wave-vector q, which is tangential in direction relative to the Corbino geometry. The dotted line shows the wave-vector $|k| = \omega/2v_{\mathrm{D}}$ where the optical excitations originally occur.

The Lorentz-force-induced current for electrons and holes at wave-vector k would cancel (since the velocities are the same) except for the relative wave-vector q induced by the OAM. This leads to an OAM-B-field induced velocity $\delta_2 u(k) = (q \cdot \nabla_k)\delta u(k) = \frac{qv_{\mathrm{D}}^2 \tau B}{k^2}(\sin 2\theta, -\cos 2\theta)$ where θ is the angle of $\vec{k}$ relative to the tangential direction $\vec{q}$. This velocity is opposite for electrons and holes so that the electron and hole components of the current now add up. The relevant current in the Corbino geometry is the radial current $I_{\mathrm{rad}} = \frac{q_e^2 R v_{\mathrm{D}}^2 (\tau_e^2 + \tau_h^2)qB}{k^2}\cos 2\theta = q_e(Rl_B^2)(2\pi l)\{(\tau_e^2 + \tau_h^2)\omega_c^2\}\cos 2\theta$. The prefactor $2q_e\pi l(Rl_B^2)$ is the ideal expectation based on angular momentum.

As shown in the figure, the radial component of the current flips sign with θ, i.e., $I_{\mathrm{rad}}(\theta \sim 0, \pi) > 0$ while $I_{\mathrm{rad}}(\theta \sim \pm\pi/2) < 0$. In fact, the straightforward average over $\cos 2\theta$ would vanish. However, for reasons we describe below, the total measured radial current $I_{\mathrm{meas}} = \int d\theta W(\theta) I_{\mathrm{rad}}(\theta)$ is a weighted average of the radial current where the presence of a $\cos 2\theta$ Fourier component of $W(\theta)$ would lead to a non-vanishing measured current.

To understand the origin of a non-trivial weight function $W(\theta)$, we note that θ represents the angle of the wave-vector k (and hence velocity) relative to the tangential direction in the Corbino geometry at which the electron-hole pair is excited. Electron-hole pairs at angles $\theta \sim \pm\pi/2$ are dominantly moving in the radial direction either towards or away from the Corbino edge. In contrast, pairs at $\theta \sim 0, \pi$ are moving tangentially. As clear from Fig. S13, the formal set of electron/hole pairs and the associated current can hit the edge on a lower time scale. This reduces the scattering time $\tau_{e,h}$ for such quasiparticles. Thus, the weight function in the radial direction $W(\theta \sim \pm\pi/2) \sim (\tau_e^{(r)} + \tau_h^{(r)})/(\tau_e + \tau_h)$, where $\tau_{e,h}^{(r)}$ is the quasiparticle scattering time for particles moving in the radial direction and $\tau_{e,h}$ is the scattering time of the quasi-particles averaged over the Fermi surface. In contrast, the tangentially moving quasiparticles have an averaged scattering time, but have a contribution to the edge conductance that is suppressed by the longitudinal conductivity $\sigma_{xx,W}$ of warm carriers. Note that the relevant conductivity is that of electron-hole pairs that are relaxing from the high optical energy scale to the ground state. The relevant weight function in the tangential direction, which arises from a current divider effect between the bulk and contact resistance, is $W(\theta \sim 0, \pi) \propto R_{\mathrm{contact}}\sigma_{xx,W}$, where R_{contact} is the contact resistance and $\sigma_{xx,W}$ is the
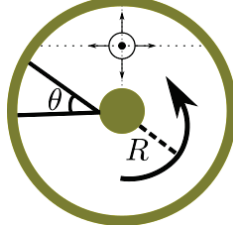
FIG. S13. Scattering in Corbino geometry. Quasiparticles moving radially towards the edge, i.e., $\theta \sim \pm\pi/2$, have a shorter scattering time resulting in smaller B-field current though can more efficiently reach the edge because of ballistic transport relative to those moving tangentially, i.e., $\theta \sim 0, \pi$.

two-dimensional conductivity (which has the same units as R_{contact}^{-1}). This is a rough qualitative estimate that may be refined by more detailed modeling of the conductivity. However, we expect the key feature of dependence on bulk conductivity to be robust.

The form of the weight function discussed above can predict a switching of sign with changing gate voltage of the measured B-dependent part of the OAM PC. As the gate voltage changes, the longitudinal conductance $\sigma_{xx,W}$ is expected to change as one passes through LLs. This leads to modulation of $W(\theta \sim \pm\pi/2)$, while one can expect $W(\theta \sim 0) \lesssim 1$ to have minor variations. At the same time $I_{\text{rad}}(\theta \sim 0, \pi) \sim -I_{\text{rad}}(\theta \sim \pi/2)$. Therefore, $I_{\text{meas}} \sim I_{\text{rad}}(\theta \sim 0, \pi)[W(\theta \sim 0, \pi) - W(\theta \sim \pm\pi/2)]$ changes sign when the bulk conductivity changes from low to high or vice-versa as the gate voltage sweeps through LLs.

[1] K. Watanabe, T. Taniguchi, and H. Kanda, Nature materials **3**, 404 (2004).

[2] F. Pizzocchero, L. Gammelgaard, B. S. Jessen, J. M. Caridad, L. Wang, J. Hone, P. Bøggild, and T. J. Booth, Nature communications **7**, 11894 (2016).

[3] B. S. Jessen, L. Gammelgaard, M. R. Thomsen, D. M. Mackenzie, J. D. Thomsen, J. M. Caridad, E. Duegaard, K. Watanabe, T. Taniguchi, T. J. Booth, *et al.*, Nature nanotechnology **14**, 340 (2019).

[4] Y. Zeng, J. Li, S. Dietrich, O. Ghosh, K. Watanabe, T. Taniguchi, J. Hone, and C. Dean, Physical review letters **122**, 137701 (2019).

[5] B. Cao, T. Grass, O. Gazzano, K. A. Patel, J. Hu, M. Müller, T. Huber-Loyola, L. Anzi, K. Watanabe, T. Taniguchi, D. B. Newell, M. Gullans, R. Sordan, M. Hafezi, and G. S. Solomon, ACS Nano **16**, 18200 (2022).

[6] M. Clifford, J. Arlt, J. Courtial, and K. Dholakia, Optics Communications **156**, 300 (1998).

[7] J. Leach, B. Jack, J. Romero, A. K. Jha, A. M. Yao, S. Franke-Arnold, D. G. Ireland, R. W. Boyd, S. M. Barnett, and M. J. Padgett, Science **329**, 662 (2010).

[8] J. Arlt, *Applications of Laguerre-Gaussian beams and Bessel beams to both nonlinear optics and atom optics*, Ph.D. thesis, University of St Andrews (2000).

[9] J. A. Davis, D. M. Cottrell, J. Campos, M. J. Yzuel, and I. Moreno, Applied optics **38**, 5004 (1999).

[10] E. Bolduc, N. Bent, E. Santamato, E. Karimi, and R. W. Boyd, Optics letters **38**, 3546 (2013).

[11] M. Goerbig, Reviews of Modern Physics **83**, 1193 (2011).

[12] F. Wendler, A. Knorr, and E. Malic, Nanophotonics **4**, 224 (2015).

[13] M. J. Gullans, J. M. Taylor, A. Imamoğlu, P. Ghaemi, and M. Hafezi, Physical Review B **95**, 235439 (2017).

[14] G. Nazin, Y. Zhang, L. Zhang, E. Sutter, and P. Sutter, Nature Physics **6**, 870 (2010).

[15] T. Grass, U. Bhattacharya, J. Sell, and M. Hafezi, Physical Review B **105**, 205202 (2022).